Journal of Astronomical Telescopes, Instruments, and Systems

AstronomicalTelescopes.SPIEDigitalLibrary.org

# Laboratory demonstration of an alternative laser guide stars wavefront sensing technique—projected pupil plane pattern

Huizhe Yang
Nazim Bharmal
Richard Myers
Eddy Younger

SPIE.

Huizhe Yang, Nazim Bharmal, Richard Myers, Eddy Younger, "Laboratory demonstration of an alternative laser guide stars wavefront sensing technique—projected pupil plane pattern," *J. Astron. Telesc. Instrum. Syst.* **5**(2), 029002 (2019), doi: 10.1117/1.JATIS.5.2.029002.

# Laboratory demonstration of an alternative laser guide stars wavefront sensing technique—projected pupil plane pattern

**Huizhe Yang,* Nazim Bharmal, Richard Myers, and Eddy Younger**
University of Durham, Department of Physics, Centre for Advanced Instrumentation, South Road, Durham, United Kingdom

**Abstract.** Adaptive optics (AO) is widely used in optical/near-infrared telescopes to remove the effects of atmospheric distortion, and laser guide stars (LGSs) are commonly used to ease the requirement for a bright, natural reference source close to the scientific target in an AO system. However, focus anisoplanatism renders single LGS AO useless for the next generation of extremely large telescopes. Here, we describe proof-of-concept experimental demonstrations of a LGS alternative configuration, which is free of focus anisoplanatism, with the corresponding wavefront sensing and reconstruction method, termed projected pupil plane pattern (PPPP). This laboratory experiment is a critical milestone between the simulation and on-sky experiment, for demonstrating the feasibility of PPPP technique and understanding technical details, such as extracting the signal and calibrating the system. Three major processes of PPPP are included in this laboratory experiment: the upward propagation, return path, and reconstruction process. From the experimental results, it has been confirmed that the PPPP signal is generated during the upward propagation and the return path is a reimaging process whose effect can be neglected (if the images of the backscattered patterns are binned to a certain size). Two calibration methods are used: the theoretical calibration is used for the wavefront measurement, and the measured calibration is used for closed-loop control. From both the wavefront measurement and closed-loop results, we show that PPPP achieves equivalent performance to a Shack–Hartmann wavefront sensor.  [DOI: 10.1117/1.JATIS.5.2.029002]

Keywords: adaptive optics; laser guide star; projected pupil plane pattern; laboratory experiment.

Paper 18122 received Dec. 1, 2018; accepted for publication Apr. 12, 2019; published online May 7, 2019.

## 1 Introduction

Adaptive optics (AO) is a technology that corrects for the effects of the atmosphere and improves the optical quality of ground-based astronomical observations.[1] However, the bright guide star required is not available across the entire sky, so laser guide stars (LGSs) are often used as a partial substitute.[2] LGSs are commonly created using a (sodium) laser, which excites sodium atoms in the mesosphere (around 90 km), forming a LGS to emit light back to the surface.[3] For a LGS AO system, the main disadvantage is that for high-altitude turbulence layers, the turbulence illuminated by the LGS will be smaller than that illuminated by the scientific target due to the finite LGS altitude. This so-called focus anisoplanatism effect becomes more pronounced for larger telescopes.[4] Laser tomography AO (LTAO) has been developed to mitigate the focus anisoplanatism, where several LGSs are generated simultaneously at different positions in the sky. Each LGS is associated with a dedicated wavefront sensor (WFS) and measurements from all WFSs are combined tomographically to estimate the 3-D turbulence.[5] However, there are some drawbacks to using LTAO. First, LTAO introduces much complexity from using multiple LGSs (e.g., six LGSs for the next generation extremely large telescopes with primary mirror diameters of over 30 m) and tomographic reconstruction, and the complexity and expense scale with the number of LGSs used.[6] Second, due to the mesospheric sodium density distribution in altitude, these LGSs produce sources elongated in the laser projection direction. The elongation consequence is that the WFS images are nonhomogeneous with perspective dependent lengthening of the LGS.[7] As this off-axis lengthening always occurs, this produces an additional measurement error within the WFS. Third, the tomographic reconstructor involved in LTAO is sensitive to the atmospheric profile $C_n^2(h)$, and varying $C_n^2(h)$ will introduce tomographic error[8] when reconstructing the 3-D atmospheric profile. Therefore, the use of multiple LGSs with elongated beacons and the associated tomography algorithms is complicated and cannot provide complete measurements of the wavefront. Thus far, their use has been limited to near-infrared observations but not used effectively at shorter wavelengths.[9]

In this paper, we test an alternative LGS configuration called projected pupil plane pattern (PPPP) and its associated wavefront sensing and reconstruction method. The PPPP technique was developed by Buscher et al.[10] as a concept in 2002 to overcome the problem of focus anisoplanatism without using the multiple-LGS-and-tomography solution. PPPP has several unique features that make it an interesting alternative to LTAO. First, turbulence is sensed during uplink, where a laser beam is projected as a collimated beam from the telescope primary mirror. This automatically eliminates the focus anisoplanatism. In addition, the power density of such collimated laser beam is significantly lower than a focused LGS, which can decrease aircraft and satellite safety hazards as it is never focused. Second, a simple camera is used to measure the wavefront by imaging the backscattered beam profiles on the sky. No WFS is needed.

*Address all correspondence to Huizhe Yang, E-mail: huizhe.yang@durham.ac.uk

2329-4124/2019/$25.00 © 2019 SPIE

Third, the wavefront reconstruction is independent of the atmospheric profile $C_n^2(h)$ and is computationally simple.

The layout of this paper is as follows. In Sec. 2, we recall the basic PPPP theory. In Sec. 3, we describe the laboratory experimental setup and the PPPP pipeline, including extracting PPPP signal and calibrating the system using theoretical and measured methods. In Sec. 4, we present the experimental results compared with a Shack–Hartmann (SH) WFS. In Sec. 5, we draw our conclusions.

## 2 PPPP Theory

PPPP is based on the transport-of-intensity equation:[11]

$$k\partial_z I = -\nabla \cdot (I\nabla\phi), \tag{1}$$

which can be approximated as Ref. 12:

$$k\frac{I_2 - I_1}{h_2 - h_1} = -\nabla \cdot (I_0\nabla\phi) = -\nabla I_0 \cdot \nabla\phi - I_0\nabla^2\phi, \tag{2}$$

where $I_0$, $I_1$, and $I_2$ are the beam profiles at the propagation distances 0, and $h_1$ and $h_2$, respectively. The turbulence phase $\phi$ is located between 0 and $h_1$. Due to $\phi$, the beam profile develops from $I_1$ to $I_2$. Thus, from $I_2 - I_1$, we can retrieve the phase $\phi$ (excluding the piston component) according to Eq. (2). The basic setup of PPPP is illustrated in Fig. 1. A laser beam is launched through the whole pupil of the telescope and propagates as a collimated beam upward through the atmosphere. When the laser pulse reaches an altitude of $h_1$, a snapshot of the Rayleigh-backscattered radiation is taken with a camera conjugate at $h_1$, which will show a disk of illumination corresponding to the telescope pupil (i.e., $I_1$). When the laser pulse reaches an altitude of $h_2$, a second snapshot is taken with another camera conjugate at $h_2$ (perhaps using the same camera with optical modulation between the two planes as in a curvature WFS setup). With the obtained $I_1$ and $I_2$, we can retrieve the turbulence phase $\phi$, according to Eq. (2). To control the propagation distance, a pulsed laser and a fast shutter are required. The symbols $\Delta h_1$ and $\Delta h_2$ represent the range gate depth for $h_1$ and $h_2$, respectively.

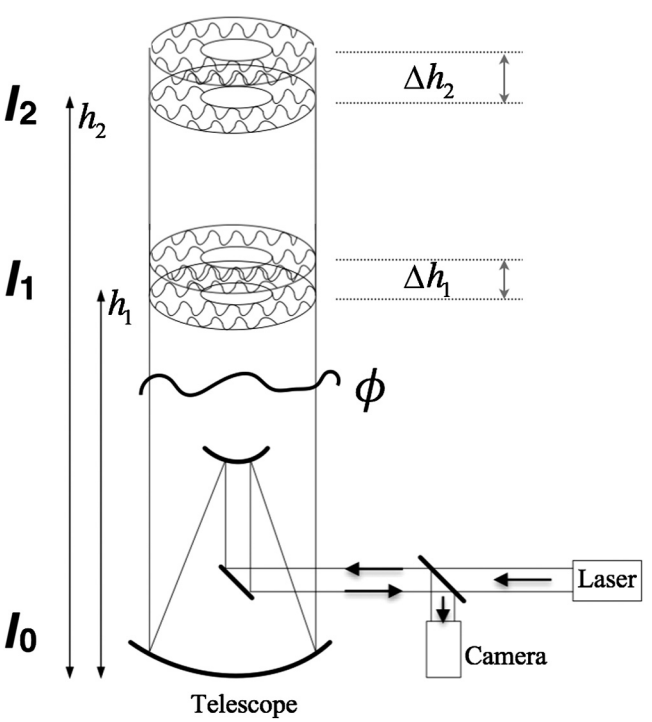


**Fig. 1** Schematic diagram of proposal PPPP on-sky configuration.

PPPP can be divided into three processes: first to propagate a collimated beam upward, through the atmospheric turbulence, from the telescope pupil plane to two altitudes—termed upward propagation; then to reimage the Rayleigh backscattered patterns at those altitudes through the same telescope by cameras conjugate at the corresponding heights—termed return path; finally to retrieve the distorted phase using the subtraction of the images from these two altitudes—termed reconstruction. Detailed description and simulation results are shown in Ref. 13. It has been demonstrated in a simulation that the required signal for PPPP is generated during the upward propagation of the collimated laser beam and the return path can be neglected if the pixel size of the binned images of the backscattered patterns is large enough.

## 3 Experimental Description

PPPP is very different from the conventional LGS AO system, in terms of the laser launching configuration, wavefront sensing technique, and reconstruction process (see Sec. 2). Similar systems have never been built either on the bench or on the sky. Thus, a laboratory demonstration is very necessary for understanding PPPP technique, including extracting PPPP signal, calibrating the system, reconstructing the phase, and how it behaves compared with a SH WFS, before putting a lot of manpower and resources into the on-sky experiment.

### 3.1 *Experimental Setup*

The optical layout of PPPP laboratory experiment is shown in Fig. 2 and an actual bench picture is included in the SPIE proceeding.[14] This setup includes propagating the laser beam to two different distances (i.e., the upward propagation) and reimaging the backscattered light from the scatter screen. The propagation distances are controlled by moving the mirror pair $M_{3a,b}$ on a rail, and the scattered light is reimaged through the same optical path back into the PPPP beam profile imaging camera. The merit of the design employed is that when moving the mirror pair from position 1 to position 2, we can simply move $f_7$ and camera 2 together and the images have the same pixel scale in terms of the beam diameter. The signal for PPPP is the subtraction of these two images (after scaling them to the same flux amount to satisfy the conservation of energy). Given the measured PPPP signal, we use a linear modal reconstruction method based on Zernike modes. A SH WFS is used as a comparison with PPPP, and camera 1 is used to record the point spread function (PSF). The relevant parameters are listed in Table 1.

The laboratory setup is a simplified demonstration to the proposal PPPP on-sky configuration (see Fig. 1) due to the limited experimental conditions, regarding the three major processes (i.e., upward propagation, return path, and reconstruction). Specifically, during the upward propagation, we use the deformable mirror (DM) or a piece of perspex of low optical quality (the lid of a container) as the atmosphere simulator. As for the return path, the scatter material (which should be the atmospheric atoms on-sky) is simplified as a reflective tape. In addition, the very significant difference between the laboratory and on-sky experiments is that the light travels through the

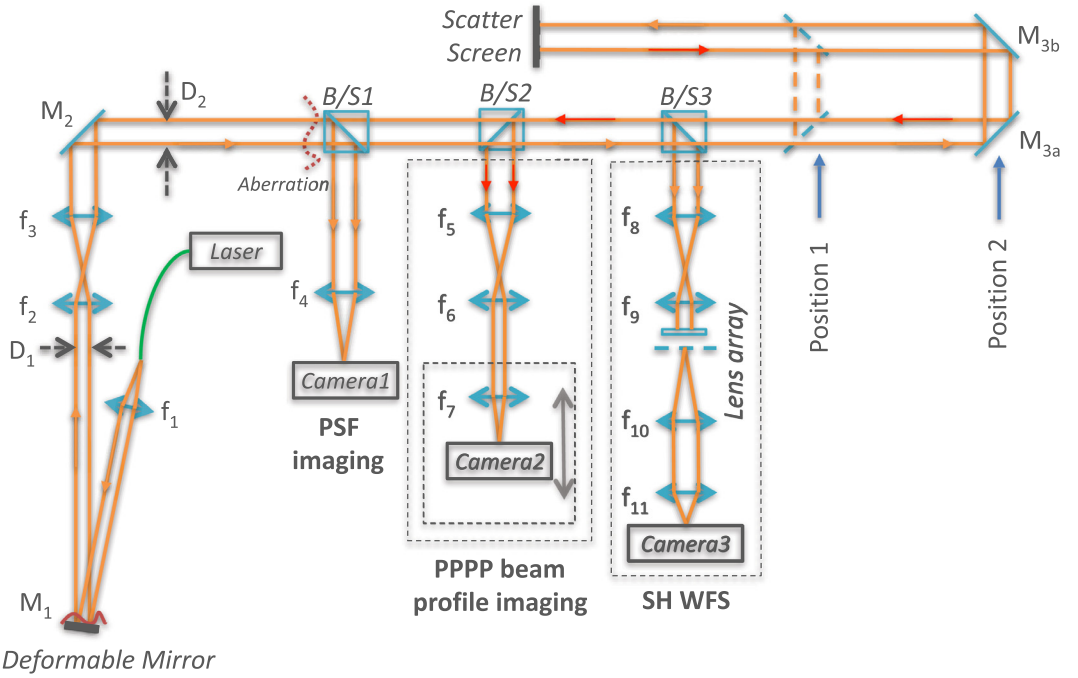


**Fig. 2** Optical layout of PPPP. A 633-nm laser beam is confined into a single-mode fiber and the other end of the fiber is mounted on a pinhole, performing as a point source. After passing through the lens $f_1$, a collimated beam is formed from the point source. The collimated beam then reaches the deformable mirror (DM). Here, the DM has two functions: one is as the atmosphere simulator to generate random aberrations (the aberration is generated on the DM and the conjugate plane is shown in the red dotted line labeled "aberration") and the other one is as a normal wavefront corrector. The DM we used is DMP40/M-P01 from Thorlabs with 40 actuators, which is suitable for generating low-order Zernike aberrations (from tip/tilt to 15th Zernike mode). $f_2$ and $f_3$ are the optical relay to change the beam diameter from $D_1$ to $D_2$. The beam is then transmitted through B/S1 (the reflected light from B/S1 goes into the camera 1), B/S2 and then is divided into two parts at B/S3. The first one (10% reflected light from B/S3) goes into the SH WFS, and the main part (90% transmission light) propagates to the scatter screen (here a reflective tape is used) via the mirror pair $M_{3a,b}$. Then, the light scatters back from the scatter screen and travels back to the PPPP beam profile imaging camera through the mirror pair again. $f_5$ and $f_6$ are another optical relay, and $f_7$ and camera 2 are used to get the image of the backscattered pattern from the scatter screen.

**Table 1** Parameters of PPPP experiment shown in Fig. 2. The unit is mm. The size of the lenslet is 10 mm × 10 mm with 500-$\mu$m pitch. The SH WFS has 9 × 9 subapertures. The two propagation distances ($h_1 = 600$ and $h_2 = 900$ mm) are equivalent to 29.6- and 44.4-km altitude for a 4-m laser beam.

| | | | | |
|---|---|---|---|---|
| $D_1 = 12$ | $D_2 = 18$ | $h_1 = 600$ | $h_2 = 900$ | $f_1 = 50$ |
| $f_2 = 100$ | $f_3 = 150$ | $f_4 = 250$ | $f_5 = 150$ | $f_6 = 75$ |
| $f_7 = 100$ | $f_8 = 100$ | $f_9 = 25$ | $f_{10} = 30$ | $f_{11} = 16$ |
| B/S2: 50:50 R:T | | B/S1 and 3: 10:90 R:T | | $\lambda = 633$ nm |

atmospheric turbulence during upward propagation and return path for the on-sky experiment, whereas in this laboratory experiment, the laser beam only passes through the atmospheric turbulence during the upward propagation process if the DM is used as the atmosphere simulator. This difference can be neglected though when the images are binned so that each pixel is larger than the downward turbulence-introduced PSF.[13] To verify this, we replace the scatter screen with a 1951 USAF target illuminated by a torch (there is no laser light here) and get the image of the target from the PPPP beam profile imaging camera, with the perspex as the atmosphere simulator. The perspex is placed at two positions: one is right after B/S2 (equivalent to 2500-m altitude for a 4-m laser beam) and the other is very close to the scatter screen. According to Yang et al.,[13] the blurring effect of $h_2$ is more severe than $h_1$; thus, we put the mirror pair at position 2 to simulate the worst case. The images of the USAF target are shown in Fig. 3 as well as the corresponding binned images. From Figs. 3(b) and 3(c), we know that the lower the turbulence layer is, the more blurred the images become. However, when the images are binned from 300 × 280 down to 30 × 28 pixels, the effect of the turbulence during the return path can be neglected [see Figs. 3(e) and 3(f)]. This reimaging test using the USAF target is consistent with the return path process of a 4-m laser beam scattered back from the altitude of 44.4 km. According to the simulation,[13] 50 × 50 pixels are maximum to sample the backscattered images to eliminate the return path effect if $h_2 = 20$ km when $r_0 = 0.15$ at 500 nm, and 30 × 30 pixels when $r_0 = 0.1$. From Fig. 3, we demonstrate that 30 × 28 pixels are sufficient to eliminate the return path effect even when $h_2 = 44.4$ km (which means more blurring effect) for this perspex as the atmosphere simulator. However, the optical effect of the perspex does not match the atmospheric statistics (such as Kolmogorov theory), so there is no $r_0$ that can be derived from it. This test then is to show the effect of the reimaging process and the effect of binning images qualitatively rather than quantitatively.

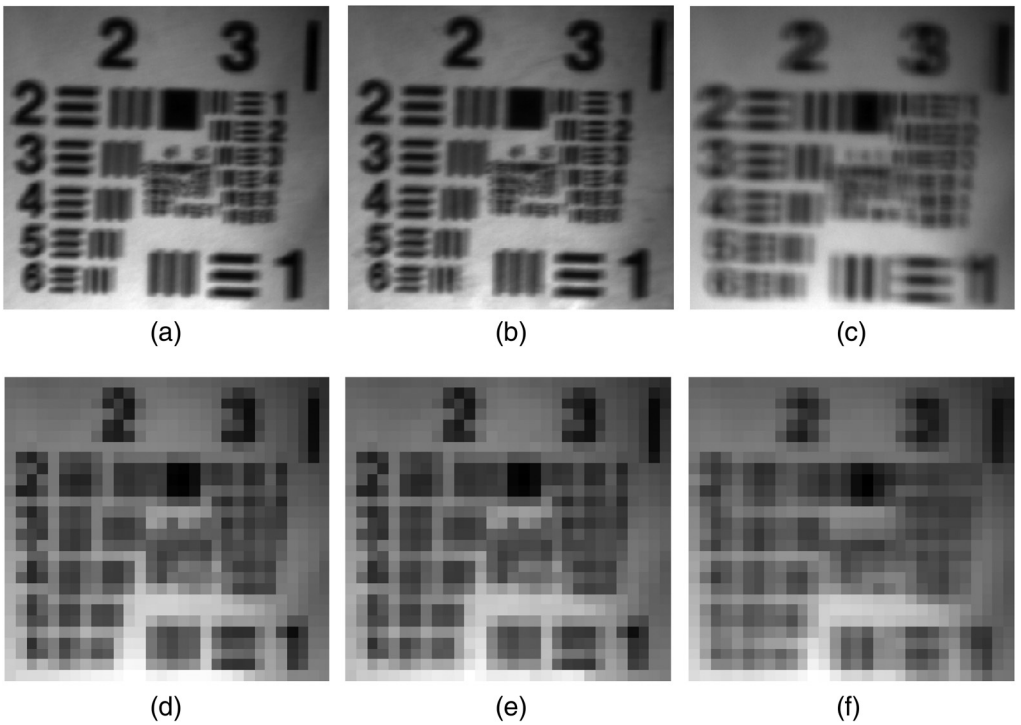


**Fig. 3** Images of the 1951 USAF target. (a) The original image of the 1951 USAF target without the perspex as the phase screen. (b) and (c) The images when the perspex is placed very close to the target (equivalent to 44.4 km altitude for a 4-m laser beam) and right after B/S2 (equivalent to 2500-m altitude for a 4-m laser beam), respectively. (d)–(f) The corresponding downsampled images from $300 \times 280$ pixels to $30 \times 28$. The size of the 1951 USAF target is $20 \times 18$ mm.

### 3.2 *PPPP Signal*

When a fixed piece of reflective tape is used as the scatter screen, the images from the PPPP camera (camera 2) are very speckled [see Fig. 4(a)] because of the diffuse reflections of laser light acting on the fixed scatter screen. In reality, the atmospheric molecules move very fast with time scale ~ several ns, whereas the atmospheric turbulence moves with time scale ~ms. So, the laser speckles will be averaged out during the "frozen" length of the turbulence. To simulate the average effect, we simply place the scatter screen on a rotating disk to average out the speckles [see Fig. 4(b)]. The structure of Fig. 4(b) is due to the diffraction effect when reflecting from the DM.

As described in Sec. 2, the PPPP signal is the subtraction of the beam profiles at $h_1$ and $h_2$, i.e., $I_1$ and $I_2$, respectively.

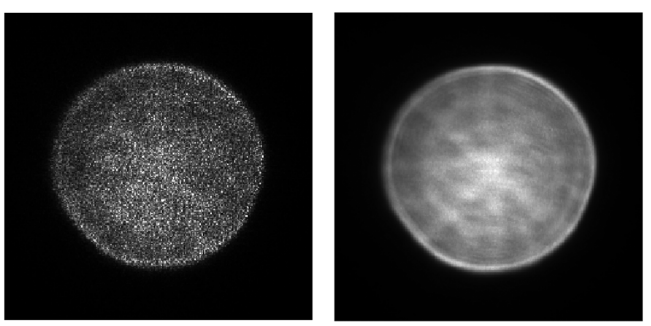


**Fig. 4** Speckled and smoothed images with rotating disk. The images are taken when the mirror pair is at position 2 and they are similar to those at position 1 although with fewer diffraction effects.

Corresponding to this laboratory experiment, $I_1$ is the image of the scattered pattern when the mirror pair is at position 1 and $I_2$ at position 2. $I_{1;0}$ and $I_{2;0}$ are the images when the DM is neutral (all the actuators are set to 100 V with range 0 to 200 V). Due to the optical static aberrations and diffraction effects, it is not possible to get zero signal from $I_{2;0} - I_{1;0}$. Thus, $I_{2;0} - I_{1;0}$ is considered as the bias signal. Then, adding a simple aberration (15th Zernike mode) from the DM, we get the corresponding images and PPPP signal (see Fig. 5). In terms of the simulated result [Fig. 5(e)], since only $I_{1;0}$ and $I_{2;0}$ are measured instead of the beam profile at the pupil $I_0$, we use Fresnel diffraction to propagate the laser beam $I_{1;0}$ [Fig. 5(a)] with distance $h_1$ to the ground, then adding a simulated 15th Zernike polynomial and propagating it back to $h_1$. In this way, the simulated image $I_1$ can be obtained and similarly for $I_2$. Then, the simulated signal is the subtraction of the simulated $I_2$ and $I_1$ [with the bias, Fig. 5(c), removed]. Comparing the simulated and measured PPPP signal [Figs. 5(e) and 5(d)], it shows great similarity on the edge but some difference in the middle. That is because the simulated 15th Zernike polynomial is different from the actual 15th Zernike mode generated from the DM. It is worth noting that the images at position 1 have a total intensity of $1.76 \times 10^6$ analog to digital units (ADU) and $2.39 \times 10^6$ ADU at position 2, which corresponds to ~1500-W laser (at 1.064 $\mu$m) for on-sky PPPP, where the altitudes of $h_1$ and $h_2$ are equal to 10 and 20 km, the optical transmission of the system is 0.5 and the quantum efficiency of the detector is 0.8. According to Yang et al.,[13] a 1500-W laser performs almost the same as a noise-free situation. Therefore, this laboratory experiment is only a proof-of-concept experiment without a complete study of the noisy situation.

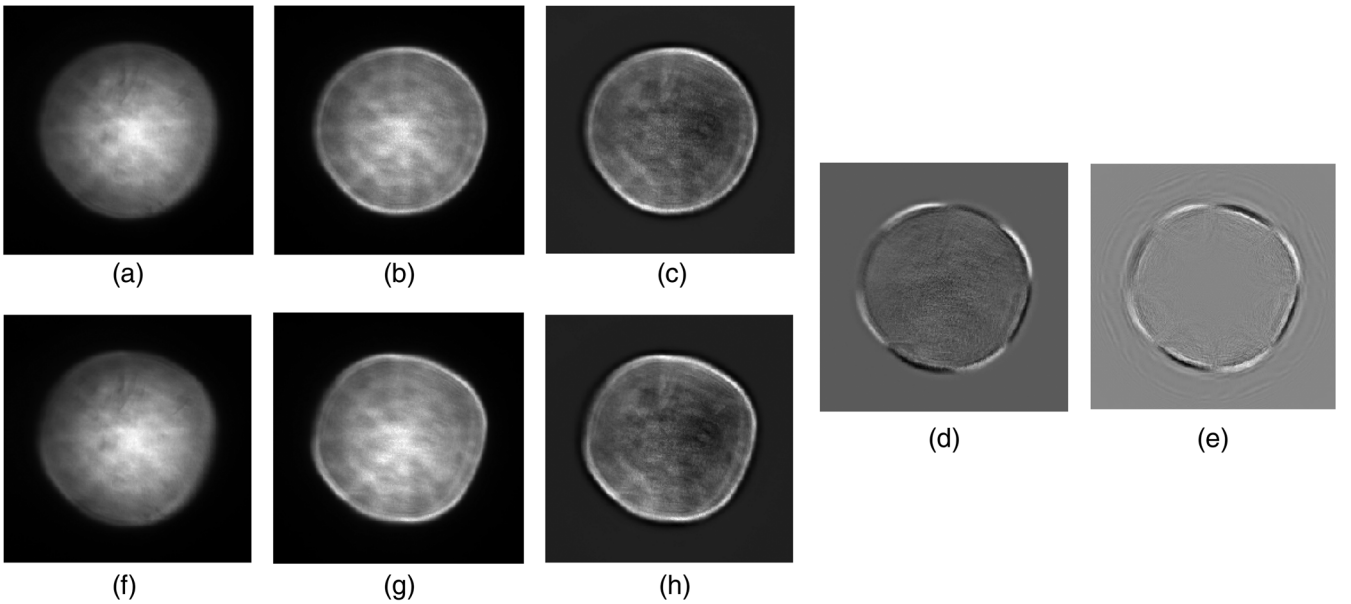


**Fig. 5** Images of backscattered patterns with neutral DM and 15th Zernike mode added on the DM. (a) and (b) Images with neutral DM at position 1 and position 2, respectively (i.e., $I_{1;0}$ and $I_{2;0}$). (c) The bias signal $I_{2;0} - I_{1;0}$. (f)–(h) The corresponding results when 15th Zernike mode (quadrafoil) is added. (d) The measured signal for 15th Zernike mode with the bias signal removed [i.e., the subtraction of (h), (c)], and (e) is the corresponding simulated result as a comparison.

### 3.3 *PPPP Calibration*

There are two approaches to PPPP calibration. One is to generate individual Zernike modes (or their approximation) by the DM (termed Zernike DM modes) and get the corresponding PPPP signal ($I_2 - I_1$), placed in a so-called interaction matrix. The other is to calculate a theoretical interaction matrix according to Yang,[13,15] given the laser beam profile at the pupil. In this paper, we use both of the calibration methods. The theoretical calibration can be theoretically calculated as long as $I_0$ is known; thus, it is fairly easy to obtain. The theoretical method is based on the Zernike polynomials[16] instead of the Zernike DM modes; thus, there exists an error when applying the reconstructed Zernike coefficients, from the theoretical calibration, to the DM directly for correction. Therefore, the theoretical calibration here is used only for the wavefront measurement experiment (instead of a full closed-loop control). The measured calibration, on the contrary, is used for the AO closed-loop control. The advantage of the measured method is that it can cancel out the static aberration from the optical system, especially the difference of the optical aberration between position 1 and position 2 when reimaging the scattered patterns. It can also connect the DM voltage command with the measured PPPP signal directly without knowing the actual wavefront.

#### 3.3.1 *Theoretical calibration*

The theoretical calibration, together with the reconstruction, is based on the Gureyev and Nugent linear method.[15] The final expression of the interaction matrix $\mathbf{M}$ is as follows:

$$M_{ij} = \int_0^{2\pi} \int_0^R I_0 \nabla Z_i \cdot \nabla Z_j r \mathrm{d}r \, \mathrm{d}\theta, \tag{3}$$

where $Z_i$ is $i$'th Zernike mode and $R$ is the radius of the laser beam. The beam profile at the pupil $I_0$ here is approximated as the average of $I_{1;0}$ and $I_{2;0}$. The reconstructed Zernike coefficient $\mathbf{a}$ corresponding to the phase $\phi$ can then be expressed as follows:

$$\mathbf{a} = kR^2 \mathbf{M}^{-1} \mathbf{F}, \tag{4}$$

where $\mathbf{F}$ is the scalar product of the measured signal with the element:

$$F_j = R^{-2} \int_0^{2\pi} \int_0^R \frac{I_2 - I_1}{h_2 - h_1} Z_j r \mathrm{d}r \, \mathrm{d}\theta. \tag{5}$$

#### 3.3.2 *Measured calibration*

For the measured calibration, each Zernike DM mode is generated twice with an equal positive and negative magnitude. The magnitudes for each Zernike DM mode to generate the measured interaction matrix are shown in Table 2. Then, the corresponding final PPPP signal is the subtraction of the PPPP signal for the positive magnitude and the PPPP signal for the negative magnitude and then divided by two. The measured interaction matrix is shown in Fig. 6. Notice that tip/tilt modes are excluded because a NGS is still needed for the tip/tilt measurement for PPPP, just as in any conventional LGS AO system. That is because the tip/tilt signal generated from the upward propagation (which is a global movement of the intensity pattern) will be affected by the return path, therefore, it is also necessary to use a natural star to provide the tip-tilt information.

#### 3.3.3 *Comparison of theoretical and measured calibration*

The theoretical interaction matrix $\mathbf{M}$ from Eq. (3) is a square matrix ($12 \times 12$) from 4th Zernike mode to 15th Zernike mode. To compare $\mathbf{M}$ with the measured interaction matrix, we calculate the correlation matrix from the measured interaction matrix

**Table 2** Magnitudes for each Zernike DM mode to generate measured interaction matrix. The unit is $\mu$m.

| $Z_j$ | 4 | 5 | 6 | 7 | 8 | 9 | 10 | 11 | 12 | 13 | 14 | 15 |
|---|---|---|---|---|---|---|---|---|---|---|---|---|
| PV | 0.65 | 0.68 | 0.68 | 0.25 | 0.25 | 0.24 | 0.24 | 0.1 | 0.11 | 0.11 | 0.21 | 0.21 |

Note: PV, peak-to-valley stroke.

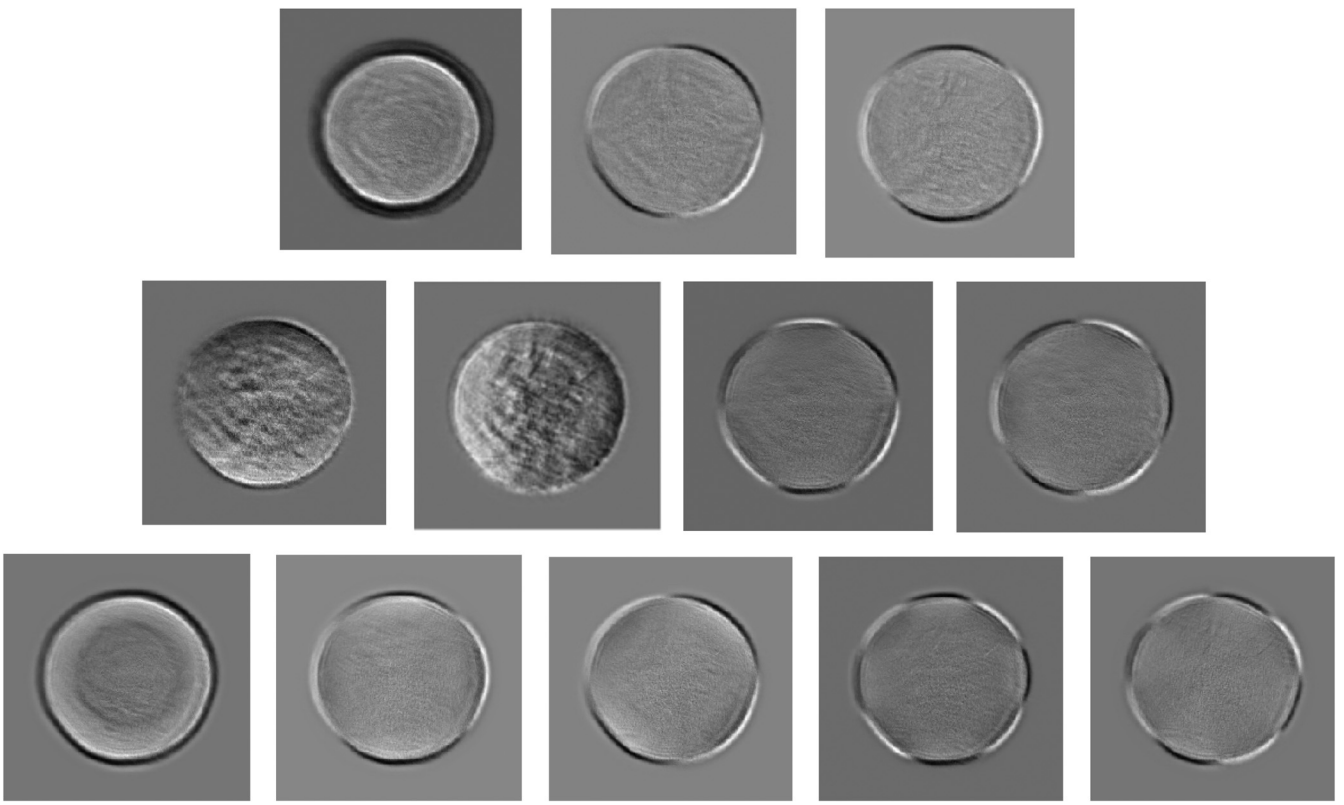

**Fig. 6** 2-D display of the measured interaction matrix for each Zernike DM mode (from 4th to 15th Zernike modes).

and the result is shown in Fig. 7. There exists a big difference between the measured correlation matrix [Fig. 7(a)] and the theoretical one [Fig. 7(b)]. It indicates again that Zernike DM modes are quite different from the simulated ones and that the correlation between each Zernike mode (for example, the 4th and 11th Zernike modes) for measured interaction matrix is much larger than the theoretical one.

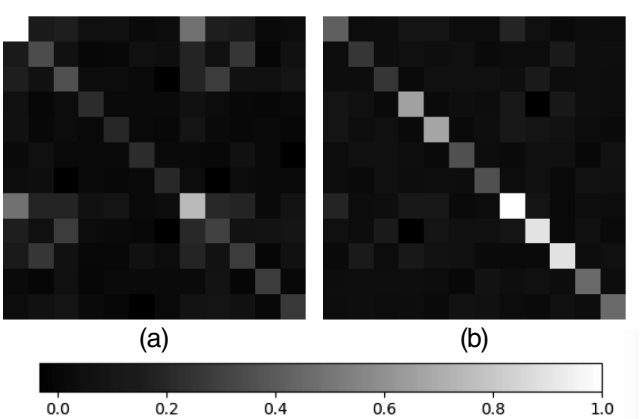


**Fig. 7** Normalized correlation matrix. (a) The correlation matrix of the measured interaction matrix and (b) the theoretical interaction matrix. Both correlation matrices are $12 \times 12$, from 4th to 15th Zernike mode.

## 4 Experimental Results

Corresponding to these two calibration methods, there are two modes for this PPPP experiment. One mode is the wavefront measurement using the theoretical calibration, where the distorted wavefront is reconstructed but no AO correction is involved. The other mode is a complete AO closed loop using the measured calibration.

### 4.1 *Wavefront Measurement*

The theoretical calibration is used for the wavefront measurement, according to Eq. (4). To verify the measurement accuracy, a SH WFS is used for comparison. Specifically, a theoretical reconstruction using Fried geometry from the SH slopes is used to reconstruct the distorted wavefront.

For the wavefront measurements, the perspex shown in Fig. 3 is used as the turbulence simulator here as well. The perspex is placed right after B/S2 (equivalent to 2500 m altitude for a 4-m laser beam). In this case, the beam goes through the turbulence

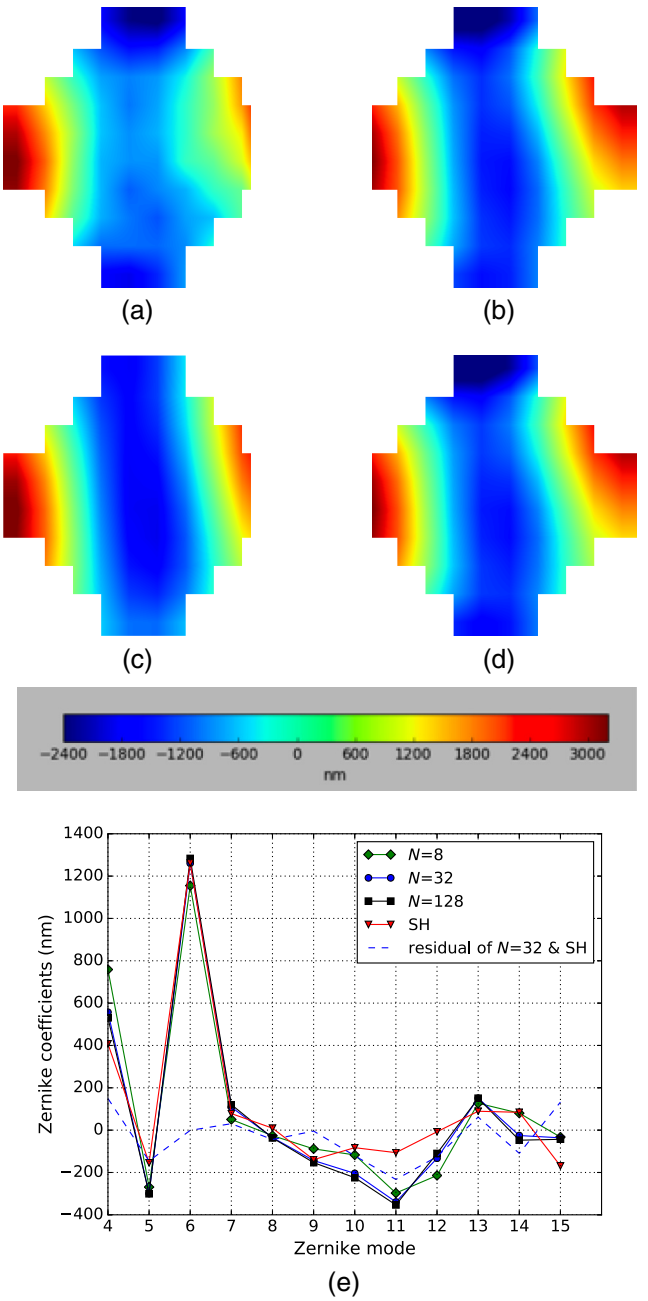


**Fig. 8** Reconstructed phases from PPPP and SH WFS using the perspex as the atmosphere simulator. (a) The reconstructed phase from the SH WFS. (b)–(d) The reconstructed phases from PPPP when the images are binned to *N* equaling 32, 8, and 128 pixels, respectively. The plots are shown on the same color scale (−2400 to 3200 nm). (e) The corresponding reconstructed Zernike coefficients.

during both the upward propagation and return path, and the blurring effect is most severe for the return path (see Fig. 3). Thus, this wavefront measurement experiment is consistent with the on-sky PPPP situation, for a worse case since the turbulence is near the ground, which has more blurring effect for the return path. Figure 8 shows the reconstructed phases from both PPPP and SH WFS. From Figs. 8(a)–8(d), we can see that the reconstructed phases from SH WFS and PPPP are very similar and that increasing the pixel number $N$ from 32 to 128 has almost no effect on the reconstructed phases because of the blurring effect of the return path, which limits the pixel number of the binned images to be $32 \times 32$ at most. In terms of the reconstructed Zernike coefficients [Fig. 8(e)], it shows again $N = 32$ and $N = 128$ are very similar to each other, as well as to the SH result, but slightly different from $N = 8$. Comparing $N = 32$ and SH WFS, the "residual of $N = 32$ and SH" curve has relatively big absolute value especially for defocus (the difference between $N = 32$ and SH is 149 nm) and spherical (232 nm). This error comes from the static aberration of the optical system, especially the difference of the optical aberration between reimaging the scattered patterns from position 1 and position 2.

### 4.2 *Closed Loop Results*

The measured calibration is used for the closed-loop control, and the DM is used as both the atmosphere simulator and wavefront corrector to perform an internal closed-loop AO system. When a random aberration is generated by the DM, we measure the images $I_1$ and $I_2$ and get the corresponding PPPP signal $I_2 - I_1$ (with the bias $I_{2;0} - I_{1;0}$ removed). Then, multiplying the PPPP signal with the control matrix (which is the pseudoinverse, from singular value decomposition, of the measured interaction matrix), we can get the reconstructed 12 Zernike DM coefficients. Applying these reconstructed Zernike DM modes on the DM, one iteration of the closed-loop control is finished. For the next iteration, only the residual aberration is measured. The voltage command applied on the DM can be expressed as $C_n = C_{n-1} + a_n \cdot g$ ($C_n$ means the absolute voltage command required for $n$'th iteration, $a_n$ represents the reconstructed Zernike DM coefficients, and $g$ is the gain), and $C_0 = 0$ (corresponding to a neutral DM, where all the actuators are set to 100 V). The closed loop is repeated for 20 iterations. Again, a SH WFS is used for comparison with similar measured calibration method, where the measured slopes are placed in an interaction matrix when each Zernike DM mode is generated.

As shown in Sec. 4.1, the binned pixel number $N$ is an important parameter for PPPP. The closed-loop gain is another key parameter for both PPPP and SH WFS for closed-loop AO system. Figure 9 shows the closed-loop results of one random aberration generated by the DM in terms of different $N$. The performance is estimated by the variance of the measured slopes as well as the variance of the actuators' voltage. The variance of the measured slopes should be close to 0 with iterations. Since the DM is used as both the aberration generator and the wavefront corrector, the variance of the actuators' voltage should approach 0. From Fig. 9, we can see that $N = 32$ gives a slightly better result after 20 iterations. The reason that $N = 32$ outperforms $N = 128$ might be that oversampling can lead to coupled error from high-order modes. Also, since the return path will introduce blurring effect and limit the pixel size $N$ to 32, we come to the choice $N = 32$. The result of SH WFS in Fig. 9 is slightly better than PPPP. Since the results are shown on a log scale, the absolute difference between PPPP and SH actually is quite small. This shows great potential for PPPP since SH WFS is a commonly used WFS for closed-loop AO. Figure 10 shows the performance of both PPPP and SH WFS in terms of different gain (only the variance of the measured slopes is shown here) when the same random aberration, as in Fig. 9, is generated on the DM. From Fig. 10, we find that the greater the gain is, the faster it converges; also, the smaller the gain is, the more stable the system becomes. As a balance, we choose the gain equaling 0.6. The measured slopes variance

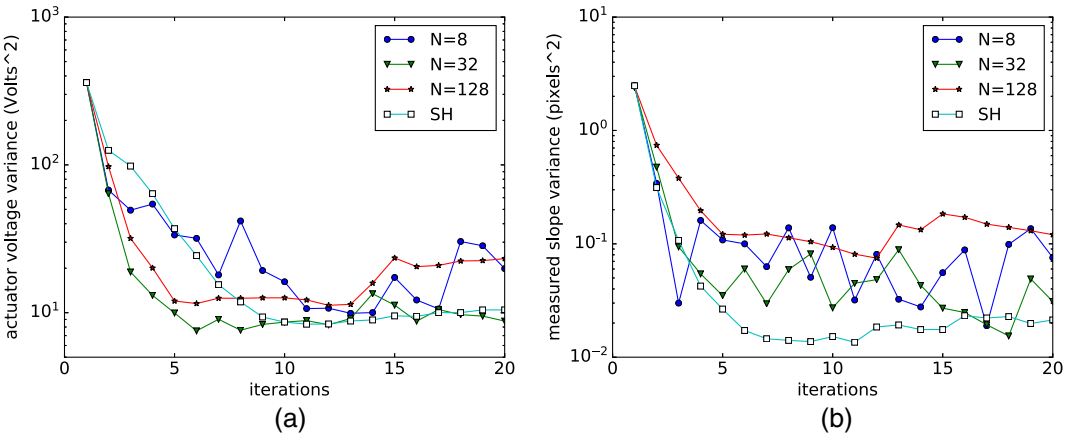


**Fig. 9** Closed-loop results in terms of different binned pixel number $N$ for a random aberration generated by the DM for both PPPP and SH WFS. (a) The variance of the measured slopes for $x$ axis and (b) the variance of the actuators' voltage.

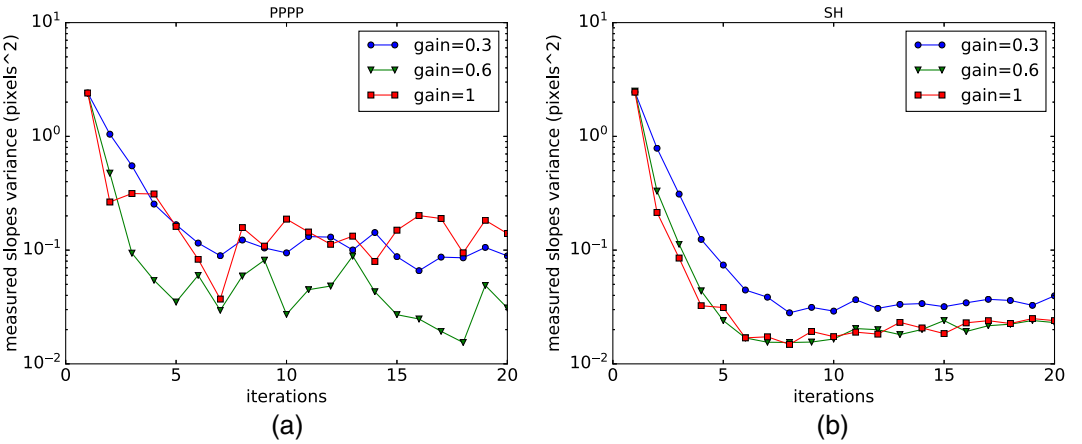


**Fig. 10** Closed-loop results in terms of closed-loop gain from the same random aberration, as shown in Fig. 9 for both PPPP and SH WFS. (a) The PPPP results and (b) the SH result. $N = 32$ is used here.

for PPPP converge to around 0.03, and it can reach 0.02 for SH WFS.

With the chosen $N = 32$ and gain $= 0.6$, Fig. 11 gives the corresponding PSFs after 20 iterations for both PPPP and SH, as well as the initial PSF we start with. From Fig. 11, we can see that after 20 iterations, the PSFs from both PPPP and SH are mostly limited inside the diffraction-limited region and improve significantly compared to the initial PSF. From Figs. 11(b) and 11(c), we can see that within 20 iterations, there is a similar higher order aberration accumulated from both PPPP and SH WFS, which means that the DM introduces some extra higher order aberrations within closed-loop iterations. These extra aberrations cannot be seen by both PPPP and SH WFS, therefore, they cannot be corrected and are accumulated. In theory, the DM should only generate a shape, which can be decomposed into 12 Zernike DM modes, as the DM commands are 12 Zernike coefficients. However, the DM apparently generates those extra higher order aberrations during iterations and causes the pattern in Figs. 11(b) and 11(c). That is because the DM shape is not the same even if the same DM voltages are added due to large hysteresis and the actual shape generated by the DM is not exactly a combination of 12 Zernike modes. Despite the imperfection of the DM, the two methods (PPPP and SH WFS) produce similar PSFs, which implies that PPPP is as good as SH WFS.

## 5 Conclusion

We have demonstrated the feasibility of a LGS alternative technique: PPPP associated with its wavefront sensing and reconstruction methods from a laboratory setup. It has been demonstrated that the PPPP signal is generated during the upward propagation and the return path can be neglected if we bin the image of the scattered patterns to $32 \times 32$ pixels. Two calibration methods are used: the theoretical one and measured calibration. The advantage of the theoretical calibration is that it can be theoretically calculated given the laser beam profile at the pupil. Thus, it is fairly easy to obtain, and a distorted wavefront can be reconstructed. The disadvantage is that it is based on the simulated Zernike polynomials; thus, the difference between the simulated and generated Zernike modes will introduce errors when trying to do a closed-loop control. In this paper, we use the theoretical calibration for the wavefront

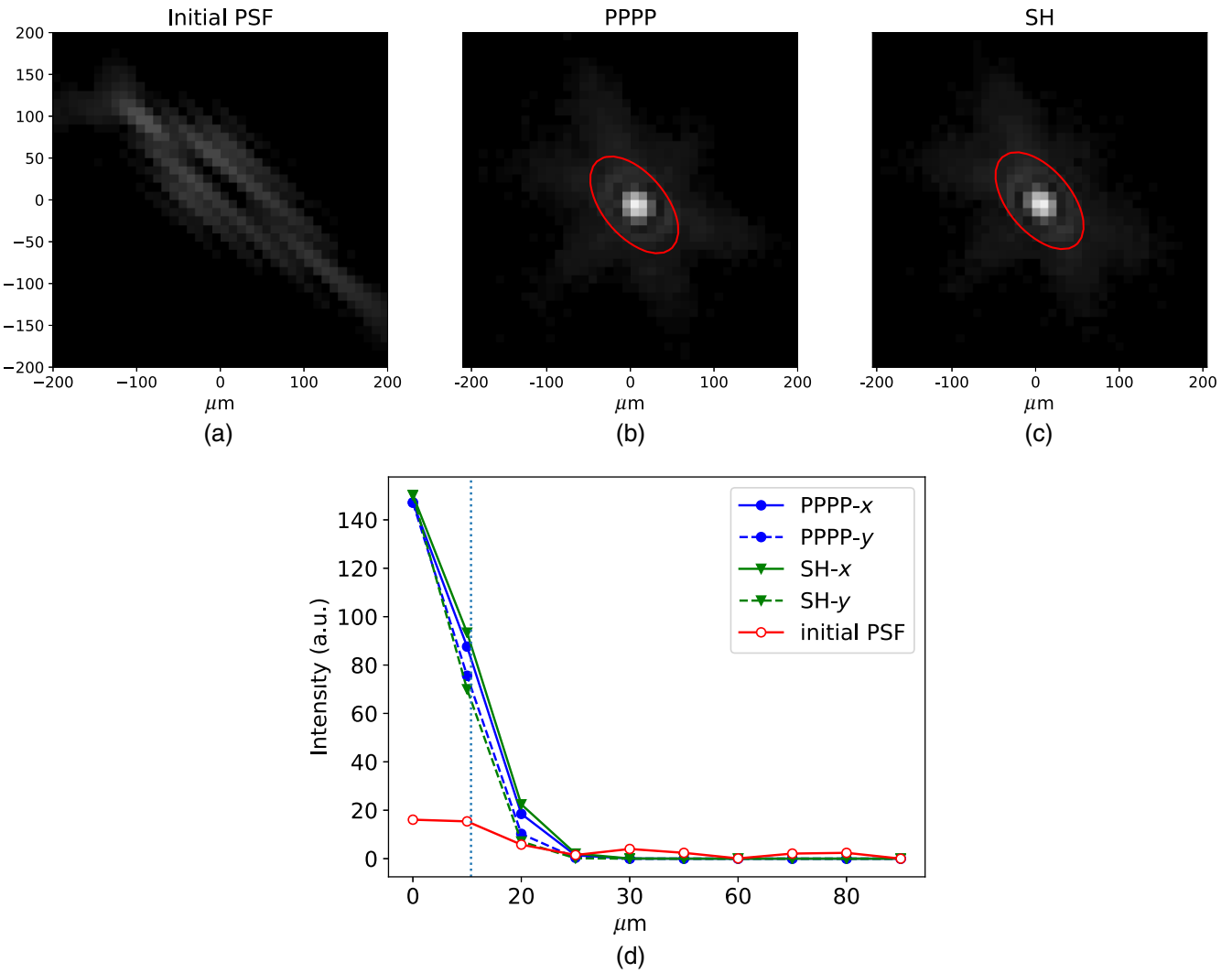


**Fig. 11** (a)–(c) Initial and corrected PSFs. The red ellipse in (b) and (c) shows a Gaussian fit. (d) The cross section of Gaussian fit along rotated "$x$" and "$y$" axis, where the FWHM can be estimated as 23.12 $\mu$m ($x$ axis) and 20.40 $\mu$m ($y$ axis) with a 41.08 deg rotation (counterclockwise) for PPPP, and 24.15 ($x$ axis) and 19.05 ($y$ axis) with a 39.38 deg rotation for SH WFS. The vertical dotted line shows the diffraction limited region, which equals to 10.72 $\mu$m.

measurement only, and the reconstructed phase shows great similarity compared with the reconstructed phase from the measured slopes of the SH WFS. As for the measured calibration, it can connect the PPPP signal directly with the DM voltage command. So, it can be used for closed loop control. We have analyzed the effect of the binned pixel number $N$ and the closed-loop gain for PPPP. From the closed-loop results of a random aberration generated by the DM, we can confirm that PPPP can achieve equivalent performance to a SH WFS.

## Acknowledgments

All authors acknowledge STFC funding ST/P000541/1. H.Y. acknowledges CSC funding.

## References

1. J. Hardy, *Adaptive Optics for Astronomical Telescopes*, Oxford University Press, Oxford (1988).
2. R. Q. Fugate et al., "Measurement of atmospheric wavefront distortion using scattered light from a laser guide-star," *Nature* **353**, 144–146 (1991).
3. L. A. Thompson and C. S. Gardner, "Experiments on laser guide stars at Mauna Kea observatory for adaptive imaging in astronomy," *Nature* **328**, 229–231 (1987).
4. D. L. Fried and J. F. Belsher, "Analysis of fundamental limits to artificial-guide-star adaptive-optics-system performance for astronomical imaging," *J. Opt. Soc. Am. A* **11**, 277–287 (1994).
5. M. Tallon and R. Foy, "Adaptive telescope with laser probe: isoplanatism and cone effect," *Astron. Astrophys.* **235**, 549–557 (1990).
6. M. L. Louarn et al., "New challenges for adaptive optics: extremely large telescopes," *Mon. Not. R. Astron. Soc.* **317**, 535–544 (2000).
7. M. Beckers, "Overcoming the perspective elongation effects in laser-guide-star-aided adaptive optics," *Appl. Opt.* **31**, 6592–6594 (1992).
8. E. Gendron et al., "Robustness of tomographic reconstructors versus real atmospheric profiles in the ELT perspective," *Proc. SPIE* **9148**, 91484N (2014).
9. P. Madec et al., "Adaptive optics facility: control strategy and first on-sky results of the acquisition sequence," *Proc. SPIE* **9909**, 99090Z (2016).

10. D. F. Buscher, G. D. Love, and R. M. Myers, "Laser beacon wavefront sensing without focal anisoplanatism," *Opt. Lett.* **27**, 149–151 (2002).
11. M. R. Teague, "Deterministic phase retrieval: a Green's function solution," *J. Opt. Soc. Am.* **73**, 1434–1441 (1983).
12. F. Roddier, "Curvature sensing and compensation: a new concept in adaptive optics," *Appl. Opt.* **27**, 1223–1225 (1988).
13. H. Yang, N. A. Bharmal, and R. M. Myers, "Projected pupil plane pattern: an alternative LGS wavefront sensing technique," *Mon. Not. R. Astron. Soc.* **477**(4), 4443–4453 (2018).
14. H. Yang et al., "LGS alternative wave-front sensing: projected pupil plane pattern (PPPP)," *Proc. SPIE* **10703**, 107030Q (2018).
15. M. R. Teague, "Phase retrieval with the transport-of-intensity equation. II. Orthogonal series solution for nonuniform illumination," *J. Opt. Soc. Am.* **73**, 1434–1441 (1983).
16. R. J. Noll, "Zernike polynomials and atmospheric turbulence," *J. Opt. Soc. Am.* **66**, 207–211 (1976).

Biographies of the authors are not available.